Adjustable Model-Based Fusion Method for Multispectral and Panchromatic Images

Liangpei Zhang, *Senior Member, IEEE*, Huanfeng Shen, *Member, IEEE*, Wei Gong, and Hongyan Zhang

***Abstract*—In this paper, an adjustable model-based image fusion method for multispectral (MS) and panchromatic (PAN) images is developed. The relationships of the desired high spatial resolution (HR) MS images to the observed low-spatial-resolution MS images and HR PAN image are formulated with image observation models. The maximum *a posteriori* framework is employed to describe the inverse problem of image fusion. By choosing particular probability density functions, the fused HR MS images are solved using a gradient descent algorithm. In particular, two functions are defined to adaptively determine most regularization parameters using the partially fused results at each iteration, retaining one parameter to adjust the tradeoff between the enhancement of spatial information and the maintenance of spectral information. The proposed method has been tested using QuickBird and IKONOS images and compared to several known fusion methods using quantitative evaluation indices. The experimental results verify the efficacy of this method.**

***Index Terms*—Adjustable image fusion, maximum a posteriori (MAP), model-based, remote sensing.**

I. Introduction

DUE TO the limits of sensor performance and/or other factors, the acquired images are often aliased and blurred. Although the single-based restoration techniques [1], [2] have the performance to increase the image definition, they only can recovery the information below the cutoff frequency determined by the diffraction limit. In order to get more image details, image fusion techniques are often used to integrate the complementary information among different images [3]–[7]. For example, multispectral (MS) images are often fused with a panchromatic (PAN) image to increase the spatial resolution.

So far, various MS/PAN fusion methods have been presented in the literature. Generally, most of the existing methods can be sorted into several basic categories: arithmetic combination methods, component-substitution methods, high-frequency information injection (HFII) methods, mixture analysis methods, model-based methods, and hybrid methods. Arithmetic combination was the earliest and simplest fusion method, based on the arithmetic computation of the PAN image and MS bands, such as the adding method, multiplication method, Brovey method, etc. [7]. The component-substitution methods are based on the transformation of the MS images into another space and the replacement of one of the newly gained components by the PAN image or by a more highly resolved image. The intensity–hue–saturation (IHS) transformation [8] and principal component analysis (PCA) [9]–[11] are the two most widely used examples. The fast spectral response function [12], University of New Brunswick (UNB) method [13], and Gram–Schmidt (GS) method [14] also belong to the component-substitution group. The HFII methods extract the high-frequency ation from the PAN image and inject them into the MS images. Ranchin and Wald called this type of methods as "ARSIS" (from its French acronym). Many HFII methods are based on multiresolution analysis such as Laplacian pyramid [15], wavelet transform [16], [17], curvelet transform [18], and contourlet transform [19]. Other HFII methods do not perform any transformation of the high frequencies before injection into MS low spatial resolution (LR) images [20], including high-pass filter [21], smoothing filter-based intensity modulation [22], etc. The Ehlers method [23] is a hybrid one which combined the IHS component-substitution and the HFII method together. Mixture analysis methods introduce spectral unmixing into the fusion process, and typical fusion methods are based on a linear mixing mode [24] and a stochastic mixing model [25].

All of the fusion methods addressed earlier do not set up an explicit relation model between the observed images and desired images. Recently, partly inspired by image restoration and superresolution reconstruction techniques [26] (another branch of image fusion), researchers have developed some model-based MS/PAN fusion methods. These methods are based on an image formulation model and regard the fusion process as an inverse optimization problem; therefore, they have stronger theoretical frameworks. In [27], Aguena and Mascarenhas use projection onto convex sets (POCS) to implement the MS/PAN fusion problem. Hardie *et al.* [28] propose a maximum *a posteriori* (MAP) method, which allows for any number of spectral bands in the primary and auxiliary image. Zhang *et al.* [29] extended this method by using wavelet-based Bayesian method to consider spatial correlation. Molina *et al.* [30] propose a variational-approximation-based fusion method following the hierarchical Bayesian framework. In [31], the spatial dependence in the MS images is learned from the PAN image using an autoregressive model, and a suitable regularization

Manuscript received July 4, 2011; revised January 17, 2012 and April 22, 2012; accepted April 27, 2012. Date of publication June 20, 2012; date of current version November 14, 2012. This work was supported in part by the Major State Basic Research Development Program (973) under Grants 2011CB707103 and 2009CB723905, by the National Natural Science Foundation of China under Grants 40971220 and 41071269, and by the National High Technology Research and Development Program (863) under Grant 2011AA120404. This paper was recommended by Editor E. Santos, Jr.

L. Zhang, W. Gong, and H. Zhang are with the State Key Laboratory of Information Engineering in Surveying, Mapping, and Remote Sensing, Wuhan University, Wuhan 430079, China (e-mail: zlp62@lmars.whu.edu.cn; weigong@lmars.whu.edu.cn; zhanghongyan@whu.edu.cn).

H. Shen is with the School of Resource and Environmental Science, Wuhan University, Wuhan 430072, China (e-mail: shenhf@whu.edu.cn).

Color versions of one or more of the figures in this paper are available online at http://ieeexplore.ieee.org.

Digital Object Identifier 10.1109/TSMCB.2012.2198810

technique is defined to enhance the resolution of MS data. More recently, the method has been further developed by incorporating inhomogeneous Gaussian Markov random field learning [32]. Li and Leung [33] developed a restoration-based MS/PAN fusion method, which uses the linear combination model of the PAN image as in [30]. Aanæs *et al.* [34] propose a method in which the image formation mode is based on the frequency composition and light intensity. Recently, Li and Yang [35] addressed the MS/PAN fusion problem from the perspective of compressed sensing theory.

In this paper, we present an adjustable model-based method for the MS/PAN fusion problem using the MAP framework. The method is based on the framework of MAP and takes full advantage of the sensor spectral response functions. More importantly, this paper presents a method to adaptively determine most regularization parameters, retaining one parameter to adjust the tradeoff between the enhancement of spatial information and the maintenance of spectral information.

The remainder of this paper is organized as follows. In Section II, the observation models of the MS and PAN images are formulated. The MAP fusion method is presented in Section III. In Section IV, the method to determine the regularization parameters is presented. The differences between the proposed method and the existed model-based methods are described in Section V. Experimental results are provided in Section VI, and Section VII concludes this paper.

II. Image Observation Models

A. Observation Model of MS Images

Let the bth band of the observed MS images be denoted in the vector form by $\boldsymbol{y}_b = [y_{b,1}, y_{b,2} \ldots, y_{b,N_1 \times N_2}]^T$, where $N_1 \times N_2$ is the image size. Letting L denote the spatial scale difference between the MS and PAN images, the underlying high spatial resolution (HR) version of $\boldsymbol{y}_b$ can be represented as $\boldsymbol{x}_b = [x_{b,1}, x_{b,2} \ldots, x_b, M_1 \times M_2]^T$ with $M_1 = L \times N_1, M_2 = L \times N_2$. The image observation model relates the desired HR image $\boldsymbol{x}_b$ to the observed LR image, and it is represented as

$$\boldsymbol{y}_b = \boldsymbol{D}\boldsymbol{S}_b\boldsymbol{x}_b + \boldsymbol{n}_b \tag{1}$$

where $\boldsymbol{S}_b$ represents the blur matrix with the size of $M_1M_2 \times M_1M_2$, $\boldsymbol{D}$ is a $N_1N_2 \times M_1M_2$ down-sampling matrix, and $\boldsymbol{n}_b$ represents the $N_1N_2 \times 1$ noise vector. Generally, $\boldsymbol{S}_b$ should be estimated using blind restoration methods. If the blurring was ignored in the fusion process, it would become an identity matrix.

For convenience, (1) can be rewritten as (2) by substituting the product of matrix $\boldsymbol{S}_b$ and $\boldsymbol{D}$ with $\boldsymbol{A}_b$

$$\boldsymbol{y}_b = \boldsymbol{A}_b\boldsymbol{x}_b + \boldsymbol{n}_b. \tag{2}$$

Thus, the full set of MS images of $\boldsymbol{y} = [\boldsymbol{y}_1^T, \boldsymbol{y}_2^T \ldots \boldsymbol{y}_B^T]^T$ and $\boldsymbol{x} = [\boldsymbol{x}_1^T, \boldsymbol{x}_2^T \ldots \boldsymbol{x}_B^T]^T$ can be related as

$$\boldsymbol{y} = \boldsymbol{A}\boldsymbol{x} + \boldsymbol{n} \tag{3}$$

where the size of $\boldsymbol{A}$ is $(N_1N_2B) \times (M_1M_2B)$ and the size of $\boldsymbol{n}$ is $(N_1N_2B) \times 1$, with B being the number of the observed MS images.

B. Observation Model of PAN Image

The second image observation model relates the desired HR MS images $\boldsymbol{x}$ to the observed HR PAN image $\boldsymbol{z}$. It has been proved that a PAN image is almost a linear combination of ideal HR MS images when the PAN band approximately covers the MS bands [33], [36], [37]. Thus, the spectral combination model can be denoted as

$$z(i,j) = \sum_{b=1}^{B} c_b x_b(i,j) + \tau + v(i,j) \tag{4}$$

where $z(i,j)$ is the brightness value of the PAN image with i and j being the positions, c_b is the corresponding weight of the bth band value $x_b(i,j)$, B is the total band number, τ is an offset, and $v(i,j)$ is the noise. Model (3) can be expressed in matrix vector form as

$$\boldsymbol{z} = \boldsymbol{C}\boldsymbol{x} + \tau\boldsymbol{I} + \boldsymbol{v}. \tag{5}$$

Here, $\boldsymbol{x} = [\boldsymbol{x}_1, \boldsymbol{x}_2 \ldots \boldsymbol{x}_B]^T$, $\boldsymbol{I}$ is the identity matrix, and $\boldsymbol{C}$ is a sparse matrix that has the following form:

$$\begin{bmatrix} c_1 & 0 & 0 & \cdots & c_2 & \cdots\cdots & c_B \\ c_1 & 0 & 0 & \cdots & c_2 & \cdots\cdots & c_B \\ & & & & & \cdots\cdots & \\ c_1 & 0 & 0 & \cdots & c_2 & \cdots\cdots & c_B \end{bmatrix}$$

where $c_1, c_2, \ldots\ldots, c_B$ can be solved using the sensor spectral response functions [33], [36], [37]. The offset τ can be approximately calculated using the down-degraded PAN image and the observed LR MS images

$$\tau = aver\left(\boldsymbol{D}\boldsymbol{z} - \sum_{b=1}^{B} c_b\boldsymbol{y}_b\right) \tag{6}$$

where $aver(\cdot)$ is the average function.

III. Map Fusion Method

A. MAP Formulation

The purpose is to realize the MAP estimate of HR MS images $\boldsymbol{x} = [\boldsymbol{x}_1, \boldsymbol{x}_2 \ldots \boldsymbol{x}_B]^T$, given the observed LR MS images $\boldsymbol{y} = [\boldsymbol{y}_1, \boldsymbol{y}_2 \ldots \boldsymbol{y}_B]^T$ and the PAN image $\boldsymbol{z}$. The estimate can be computed by

$$\hat{\boldsymbol{x}} = \arg\max_{\boldsymbol{x}} p(\boldsymbol{x}|\boldsymbol{y}, \boldsymbol{z}). \tag{7}$$

Applying Bayes' rule, (6) becomes

$$\hat{\boldsymbol{x}} = \arg\max_{\boldsymbol{x}} \frac{p(\boldsymbol{x})p(\boldsymbol{y}, \boldsymbol{z}|\boldsymbol{x})}{p(\boldsymbol{y}, \boldsymbol{z})}. \tag{8}$$

Since $p(\boldsymbol{y},\boldsymbol{z})$ is independent of $\boldsymbol{x}$, it can be considered a constant and removed from the maximum function

$$\begin{aligned}\hat{\boldsymbol{x}} &= \arg\max_{\boldsymbol{x}} p(\boldsymbol{x})p(\boldsymbol{y},\boldsymbol{z}|\boldsymbol{x}) \\ &= \arg\max_{\boldsymbol{x}} p(\boldsymbol{x})p(\boldsymbol{y}|\boldsymbol{x})p(\boldsymbol{z}|\boldsymbol{x},\boldsymbol{y}) \\ &= \arg\max_{\boldsymbol{x}} p(\boldsymbol{x})p(\boldsymbol{y}|\boldsymbol{x})p(\boldsymbol{z}|\boldsymbol{x}). \end{aligned} \tag{9}$$

Since $\boldsymbol{z}$ and $\boldsymbol{y}$ are both known quantities, therefore, it is tenable for $p(\boldsymbol{z}|\boldsymbol{x},\boldsymbol{y}) = p(\boldsymbol{z}|\boldsymbol{x})$ in (9).

B. Fusion Model

It is seen that there are three probability density functions in (9). The function $p(\boldsymbol{y}|\boldsymbol{x})$ provides a measure of the conformance of the estimated image $\boldsymbol{x}$ to the observed image $\boldsymbol{y}$ according to the observation model (3). It is determined by the probability density of the noise vector, i.e.,

$$p(\boldsymbol{y}|\boldsymbol{x}) = \frac{1}{\sqrt{(2\pi)^{N_1N_2\times B}|\boldsymbol{K}|}} \exp\left\{-\frac{1}{2}(\boldsymbol{y}-\boldsymbol{A}\boldsymbol{x})\boldsymbol{K}^{-1}(\boldsymbol{y}-\boldsymbol{A}\boldsymbol{x})\right\} \tag{10}$$

where $\boldsymbol{K}$ is the covariance matrix that describes the noise $\boldsymbol{n}$. As in [31]–[33] and [35], this paper models the noise as independent and identically distributed from pixel to pixel. However, we assume that the distribution is independent and nonidentical from band to band. In this case, the matrix $\boldsymbol{K}$ is diagonal with the elements being noise variances of the corresponding bands. Thus, (10) can be simplified to

$$p(\boldsymbol{y}|\boldsymbol{x}) = \prod_{b=1}^{B} \frac{1}{(2\pi\alpha_b)^{N_1N_2/2}} \exp\left\{-\|\boldsymbol{y}_b - \boldsymbol{A}_b\boldsymbol{x}_b\|^2/2\alpha_b\right\} \tag{11}$$

where α_b is the variance of the noise $\boldsymbol{n}_b$.

The function $p(\boldsymbol{z}|\boldsymbol{x})$ is determined by the probability density of the noise vector $\boldsymbol{v}$ in (5) and is expressed as

$$p(\boldsymbol{z}|\boldsymbol{x}) = \frac{1}{(2\pi\beta)^{M_1M_2/2}} \exp\left\{-\|\boldsymbol{z} - \boldsymbol{C}\boldsymbol{x} - \tau\boldsymbol{I}\|^2/2\beta\right\} \tag{12}$$

where β is the variance of the noise $\boldsymbol{v}$.

The density function $p(\boldsymbol{x})$ models the image prior. Although some cross-channel models have been tried as in [38] and [39] in our experiments, the image equality of the fused images does not have a considerable improvement with the increase of computational complexity. One possible reason is that different MS bands have been correlated by (12). Therefore, this paper models the image prior independently for each band. The Laplacian prior has been used for the fusion problem in [30] and [33]. However, this prior often leads to some high-frequency energy in the image being removed [40].Therefore, an edge-preserving Huber–Markov image model [41] is employed as

$$p(\boldsymbol{x}) = \prod_{b=1}^{B} \frac{1}{(2\pi\gamma_b)^{M_1M_2/2}} \times \exp\left\{-\sum_{i,j}\sum_{\boldsymbol{\xi}\in\psi} \rho\left(d_{\boldsymbol{\xi}}\left(\boldsymbol{x}_b(i,j)\right)\right)/2\gamma_b\right\} \tag{13}$$

where γ_b is the model parameter of the bth band, ξ is a local group of pixels called a clique, and ψ is the set of all the cliques. The quantity $d_\xi(x_b(i,j))$ is a spatial activity measure to pixel $x_b(i,j)$, and the following finite second-order differences are computed in two adjacent cliques for every location (i,j) in the image

$$d^1_{\boldsymbol{\xi}}\left(x_b(i,j)\right) = x_b(i-1,j) - 2x_b(i,j) + x_b(i+1,j) \tag{14}$$

$$d^2_{\boldsymbol{\xi}}\left(x_b(i,j)\right) = x_b(i,j-1) - 2x_b(i,j) + x_b(i,j+1). \tag{15}$$

In (13), $\rho(\cdot)$ is the Huber function defined as

$$\rho(h) = \begin{cases} h^2 & |h| \le \mu \\ 2\mu|h| - \mu^2 & |h| > \mu \end{cases} \tag{16}$$

where μ is a threshold parameter separating the quadratic and linear regions. When μ approaches $+\infty$, the prior becomes the Gauss–Markov, which has similar spatial constraints to the Laplacian prior used in [30].

Substituting (11)–(13) in (9) and implementing the monotonic logarithm function, after some manipulation, N_1, N_2, M_1, and M_2 can be safely dropped, and the maximization of this posterior probability distribution is equivalent to the following regularized minimum problem:

$$\hat{\boldsymbol{x}} = \arg\min\left[E(\boldsymbol{x})\right] \tag{17}$$

where

$$\begin{aligned} E(\boldsymbol{x}) = &\sum_{b=1}^{B} \lambda_{b,1}\|\boldsymbol{y}_b - \boldsymbol{A}_b\boldsymbol{x}_b\|^2 + \|\boldsymbol{z} - \boldsymbol{C}\boldsymbol{x} - \tau\boldsymbol{I}\|^2 \\ &+ \sum_{b=1}^{B} \lambda_{b,2} \sum_{i,j}\sum_{\boldsymbol{\xi}\in\psi} \rho\left(d_{\boldsymbol{\xi}}\left(\boldsymbol{x}_b(i,j)\right)\right). \end{aligned} \tag{18}$$

In (18), $\lambda_{b,1} = \beta/\alpha_b$ and $\lambda_{b,2} = \beta/\gamma_b$ are regularization parameters. It is noted that the regularization parameters balance the relative contributions of the different terms. Since there have been regularization parameters in the first and the third terms, the relative contribution of the middle term can also be balanced by these parameters. Therefore, there is no need for an additional parameter.

C. Optimization Method

The gradient descent method is employed to solve the fusion images. Differentiating (18) with respect to $\boldsymbol{x}_b$, we have

$$\begin{aligned} \nabla E(\boldsymbol{x}_b) = &-2\lambda_{b,1}\boldsymbol{A}_b^T(\boldsymbol{y}_b - \boldsymbol{A}_b\boldsymbol{x}_b) - 2c_b(\boldsymbol{z} - \boldsymbol{C}\boldsymbol{x} - \tau\boldsymbol{I}) \\ &+2\lambda_{b,2}\boldsymbol{G}^T\rho'(\boldsymbol{G}\boldsymbol{x}_b) \end{aligned} \tag{19}$$

where $\boldsymbol{G}\boldsymbol{x}_b$ is a vector comprising all elements of clique set $\boldsymbol{\psi}$ with $\boldsymbol{G}$ being the corresponding large sparse matrix. The corresponding gradient element of the prior term is given by

$$\rho'(h) = \begin{cases} 2h & |h| \le \mu \\ 2\mu \text{ sign } (h) & |h| > \mu \end{cases}. \tag{20}$$

Thus, the HR image $\boldsymbol{x}_b$ can be solved by employing the successive approximation iteration

$$\hat{\boldsymbol{x}}_{b,n+1} = \hat{\boldsymbol{x}}_{b,n} - \beta_n \nabla E(\hat{\boldsymbol{x}}_{b,n}) \tag{21}$$

where n is the iteration number and β_n is the step size. By making a second-order Taylor series approximation to the objective function at the current state $\hat{\boldsymbol{x}}_n$, a quadratic step size approximation becomes (22) shown at the bottom of the page, where $\boldsymbol{H}_b$ is the Hessian matrix of $\sum_{i,j}\sum_{\boldsymbol{\xi}\in\psi}\rho(d_{\boldsymbol{\xi}}(\boldsymbol{x}_b(i,j)))$. In each iteration, the MS images are updated one by one. The iteration is terminated when

$$\|\hat{\boldsymbol{x}}_{n+1} - \hat{\boldsymbol{x}}_n\|^2 / \|\hat{\boldsymbol{x}}_n\|^2 \le d \tag{23}$$

where d is a predetermined coefficient.

IV. Determination of Regularization Parameters

To implement the MAP fusion described earlier, $2B$ regularization parameters of $\lambda_{b,1}$ and $\lambda_{b,2}(b = 1, 2 \ldots B)$ should be determined, and these parameters are controlled by the variances α_b, β, and γ_b. In most cases, it is difficult or impossible to obtain an accurate estimate of such variances. The best way to solve the problem is to look for a method to adaptively determine all the $2B$ parameters. In MS/PAN fusion, however, there is a tradeoff between the enhancement of spatial information and the maintenance of spectral information. Different remote sensing applications may expect different fusion results. Therefore, some adjustable methods have been proposed to control over how much spatial detail or spectral information should be retained [42], [43].

This paper proposes an alternative method to solve the problem of parameter determination. Rewriting (18) as

$$E(\boldsymbol{x}) = \lambda_{\text{tradeoff}} \sum_{b=1}^{B} \lambda'_{b,1} \|\boldsymbol{y}_b - \boldsymbol{A}_b\boldsymbol{x}_b\|^2 + \|\boldsymbol{z} - \boldsymbol{C}\boldsymbol{x} - \tau\boldsymbol{I}\|^2 + \sum_{b=1}^{B} \lambda_{b,2} \sum_{i,j} \sum_{\boldsymbol{\xi}\in\psi} \rho\left(d_{\boldsymbol{\xi}}\left(\boldsymbol{x}_b(i,j)\right)\right) \tag{24}$$

where $\lambda_{\text{tradeoff}} = \lambda_{b,1}/\lambda'_{b,1}$ is regarded as an adjustable parameter between the enhancement of spatial information and the maintenance of spectral information, the $2B$ parameters of $\lambda'_{b,1}$ and $\lambda_{b,2}(b = 1, 2 \ldots B)$ are determined adaptively. In the literature, the generalized cross-validation (GCV) [44], L-curve [45], U-curve [46], [47], and variational-approximation [30] methods have been used for parameter determination in ill-posed inverse problems. These methods often need complicated mathematical calculations. For example, the calculation of trace of some matrix is inevitable in the GCV method, which requires the construction of the large sparse matrices in (24). In this paper, the large sparse matrices are interpreted as direct image operators to relieve the computation load. Inspired by [48]–[50], therefore, this paper proposes to determine $\lambda'_{b,1}$ and $\lambda_{b,2}$ by designing appropriate functions of the partially fused images and updating them at each iteration. The main challenge is that two series of regularization parameters should be adaptively determined because of the incorporation of a spectral residual term in the MS/PAN fusion problem.

A. Determination of $\lambda'_{b,1}$

The regularization parameter $\lambda'_{b,1}$ should be selected in such a way that each individual cost function is convex and it is able to control the balance of residual terms $\|\boldsymbol{y}_b - \boldsymbol{A}_b\boldsymbol{x}_b\|^2$ in different bands. Based on the regularization theory, the first property that it should satisfy is $\lambda'_{b,1} \ge 0$ for any band. Second, since $\lambda'_{b,1}$ is actually a relative weight of the bth band, we assume that the average of all bands is 1, i.e., $\sum_{b=1}^{B} \lambda'_{b,1} = B$. Third, based on the set theoretic formulation, $\lambda'_{b,1}$ should be set as a larger value to increase the contribution of $\|\boldsymbol{y}_b - \boldsymbol{A}_b\boldsymbol{x}_b\|^2$ in the next iteration when its current energy value is smaller, and vice versa [48]–[50]. Thus, $\lambda'_{b,1}$ is inversely proportional to $\|\boldsymbol{y}_b - \boldsymbol{A}_b\boldsymbol{x}_b\|^2$. According to these recognitions, we define the function as

$$\lambda'_{b,1} = B \cdot \frac{1/\log\left(1 + \|\boldsymbol{y}_b - \boldsymbol{A}_b\boldsymbol{x}_b\|^2\right)}{\sum_{b=1}^{B}\left[1/\log\left(1 + \|\boldsymbol{y}_b - \boldsymbol{A}_b\boldsymbol{x}_b\|^2\right)\right]}. \tag{25}$$

Here, the $\log(\cdot)$ function prevents the parameter from being too sensitive to the partially reconstructed image $\hat{\boldsymbol{x}}_b$, and the value 1 in the variable part of the $\log(\cdot)$ function ensures the condition of $\lambda'_{b,1} \ge 0$.

B. Determination of $\lambda_{b,2}$

The function of $\lambda_{b,2}$ is using $E_3 = \sum_{i,j}\sum_{\boldsymbol{\xi}\in\psi}\rho(d_{\boldsymbol{\xi}}(\boldsymbol{x}_b(i,j)))$ to improve the instability problem caused by $E_{1,2} = \lambda_{b,1}\|\boldsymbol{y}_b - \boldsymbol{A}_b\boldsymbol{x}_b\|^2 + \|\boldsymbol{z} - \boldsymbol{C}\boldsymbol{x} - \tau\boldsymbol{I}\|^2$. Therefore, a feasible way to determine $\lambda_{b,2}$ is to update it at each iteration using $E_{1,2}$ and E_3 with respect to the partially reconstructed image $\hat{\boldsymbol{x}}_b$, i.e.,

$$\lambda_{b,2} = f(E_{1,2}, E_3). \tag{26}$$

First, the smaller the norm E_3, the more energy is distributed to the low frequency components in the partially reconstructed image, and a relatively smaller regularization parameter can be

$$\beta_n = \frac{\sum_{b=1}^{B}\left[\nabla E(\hat{\boldsymbol{x}}_{b,n})\right]^T \nabla E(\hat{\boldsymbol{x}}_{b,n})}{\sum_{b=1}^{B}\left[\nabla E(\hat{\boldsymbol{x}}_{b,n})\right]^T \left[\lambda_{b,1}\boldsymbol{A}_b^T\boldsymbol{A}_b + \lambda_{b,2}\boldsymbol{H}_b\right] \nabla E(\hat{\boldsymbol{x}}_{b,n}) + \left[\sum_{b=1}^{B} c_b \nabla E(\hat{\boldsymbol{x}}_{b,n})\right]^T \left[\sum_{b=1}^{B} c_b \nabla E(\hat{\boldsymbol{x}}_{b,n})\right]} \tag{22}$$

used to further recover high-frequency components, and vice versa [50]. Second, a larger $E_{1,2}$ represents a larger model error, and a relatively larger $\lambda_{b,2}$ can be used to strengthen the spatial constraint. Therefore, $\lambda_{b,2}$ should be proportional to both $E_{1,2}$ and E_3. In this paper, it is assumed to have the form

$$\lambda_{b,2} = \frac{\lambda_{b,1}\|\boldsymbol{y}_b - \boldsymbol{A}_b\boldsymbol{x}_b\|^2 + \|\boldsymbol{z} - \boldsymbol{C}\boldsymbol{x} - \tau\boldsymbol{I}\|^2}{\chi_b - \sum_{i,j}\sum_{\boldsymbol{\xi}\in\psi}\rho\left(d_{\boldsymbol{\xi}}\left(\boldsymbol{x}_b(i,j)\right)\right)} \tag{27}$$

where χ_b is a parameter related to the image $\boldsymbol{y}_b$ or $\boldsymbol{x}_b$. In order to ensure $\lambda_{b,2} > 0$, χ_b should be larger than $\sum_{i,j}\sum_{\boldsymbol{\xi}\in\psi}\rho(d_{\boldsymbol{\xi}}(\boldsymbol{x}_b(i,j)))$. Our experiments indicate that $\chi_b = \|\boldsymbol{y}_b\|^2$ is a good choice for most cases.

V. Difference With Other Model-Based Methods

During recent years, several model-based methods have been proposed [27]–[35]. With the exception of the method in [27], which employs the POCS framework, most methods are based on a Bayesian or regularization framework. Similarly, these methods are based on some image models and regard the fusion process as an inverse optimization problem. Generally, there are two types of image models that can be used. One relates the HR MS images $\boldsymbol{x}$ to the LS MS images $\boldsymbol{y}$, and the other relates $\boldsymbol{x}$ to the observed HR PAN image $\boldsymbol{z}$. In this paper, (3) and (5) respectively correspond to these two types of image models.

In some references, only the first type of image model is used. In [31] and [32], for example, the energy function of the fusion model is

$$E(\boldsymbol{x}) = \lambda\sum_{b=1}^{B}\|\boldsymbol{y}_b - \boldsymbol{A}_b\boldsymbol{x}_b\|^2 + \sum_{b=1}^{B}U(\boldsymbol{x}_b) \tag{28}$$

where $U(\boldsymbol{x}_b)$ is either an inhomogeneous Gaussian Markov model or an autoregressive model. Here, the original PAN image $\boldsymbol{z}$ is not included in the fusion model but is used to learn the parameters in $U(\boldsymbol{x}_b)$. This model is based on the assumption that all MS bands have similar spatial structures to the PAN image. The methods in [28] and [29] also never use the second type of image model. More distinctly, the derived Bayesian equation

$$\hat{\boldsymbol{x}} = \arg\max_{\boldsymbol{x}} p(\boldsymbol{y}|\boldsymbol{x})p(\boldsymbol{x}|\boldsymbol{z}) \tag{29}$$

used in these references is greatly different from (9) in this paper. Moreover, in [28], [29], [31], and [32], the sensor spectral response function that plays an important role in our method is never used.

Some other methods employ both types of image models but use a simplified parameter set. For example, the parameters $\lambda_{b,1}$ and $\lambda_{b,2}$ in (18) are assumed invariant in different bands, and $\lambda_{b,1}$ is set to 1 in [33] and [35]. Thus, the fusion model becomes

$$E(\boldsymbol{x}) = \sum_{b=1}^{B}\|\boldsymbol{y}_b - \boldsymbol{A}_b\boldsymbol{x}_b\|^2 + \lambda\sum_{b=1}^{B}\sum_{i,j}\sum_{\boldsymbol{\xi}\in\psi}\rho\left(d_{\boldsymbol{\xi}}\left(\boldsymbol{x}_b(i,j)\right)\right) + \|\boldsymbol{z} - \boldsymbol{C}\boldsymbol{x} - \tau\boldsymbol{I}\|^2. \tag{30}$$

This choice presumes that $\boldsymbol{n}_b$ in (2) and $\boldsymbol{v}$ in (5) have the same standard deviation. However, it is obvious that this assumption is not satisfied in many cases. Furthermore, the restoration-based fusion method in [33] does not consider the down-sampling matrix $\boldsymbol{D}$ in the observation model, and the interpolated versions of MS images are directly used in the fusion process. The advantages of the proposed method are validated in the experiment section.

The method in [34] ignores the direct physical relations embodied in the two types of image models. Alternatively, the relations between $\boldsymbol{z}$, $\boldsymbol{y}_b$ and $\boldsymbol{x}_b$ are expressed in one empirical equation

$$\boldsymbol{x}_b = \boldsymbol{y}_b + \alpha_{x_b,z}\left(\boldsymbol{z} - mean(\boldsymbol{z})\right) \tag{31}$$

where $mean(\boldsymbol{z})$ denotes the mean of the HR pixels in the scope of one LR pixel and the parameter $\alpha_{x_b,z}$ denotes the cosine of the angle between $\boldsymbol{x}_b$ and $\boldsymbol{z}$.

In this paper, two functions are defined to adaptively determine most of the regularization parameters. In [30], the adaptive determination of model parameters in the fusion problem is also researched using a variational distribution approximation technique. This method needs very complicated mathematical calculations, whereas our proposed method is much more computationally simple. Moreover, the proposed method retains one parameter to adjust the tradeoff between the enhancement of spatial information and the maintenance of spectral information. The adjustable fusion technique can make the method more applicable to different remote sensing applications. In order to avoid the image being oversmoothed, this paper employs an edge-persevering Huber–Markov prior model. The advantage of this model is also validated in the experiment section.

VI. Experimental Results

In the experiments, we tested the proposed algorithm using QuickBird and IKONOS images. In order to evaluate the fused images, two properties need to be checked [33], [51], [52]. The first is the *synthesis* property that any fused image (or MS set of images) should be as identical as possible to the image (or MS set of images) that the corresponding sensor would observe with the highest spatial resolution. As there is no reference image available at high spatial resolution, a commonly used evaluation method is to resample the original PAN and MS images down to an inferior resolution level and then treat the original MS images as the real high-resolution images to compare with the synthesized images. The second is the *consistency* property that any fused image (or MS set of images), once degraded to its original resolution, should be as identical as possible to the original LR image (or MS set of images). This property is often used for the validation of spectral fidelity when the fusion method is performed on real observed images.

A. Experiments on Simulated Images

In the simulated experiments, the proposed method and several typical existed fusion methods are compared in terms

of the *synthesis* property. The fused images are evaluated using five quality indices. These are the root-mean-square error (rmse), correlation coefficient (CC), universal image quality index (UIQI), relative dimensionless global error in synthesis (ERGAS), and spectral angle (SA). They are defined by (28)–(32), respectively

$$\mathrm{rmse}_b = \sqrt{\frac{\|\hat{\boldsymbol{x}}_b - \boldsymbol{x}_b\|^2}{M_1 M_2}} \tag{32}$$

$$\mathrm{CC}_b = \frac{\sigma_{\hat{\boldsymbol{x}}_b \boldsymbol{x}_b}}{\sigma_{\hat{\boldsymbol{x}}_b} \sigma_{\boldsymbol{x}_b}} \tag{33}$$

$$\mathrm{UIQI}_b = \frac{4\sigma_{\hat{\boldsymbol{x}}_b \boldsymbol{x}_b} m_{\hat{\boldsymbol{x}}_b} m_{\boldsymbol{x}_b}}{\left(\sigma^2_{\hat{\boldsymbol{x}}_b} + \sigma^2_{\boldsymbol{x}_b}\right)\left(m^2_{\hat{\boldsymbol{x}}_b} + m^2_{\boldsymbol{x}_b}\right)} \tag{34}$$

$$\mathrm{ERGAS} = 100 \cdot L \cdot \sqrt{\frac{1}{B}\sum_{b}^{B} \frac{\mathrm{MSE}_b}{m^2_{\boldsymbol{x}_b}}} \tag{35}$$

$$\mathrm{SA} = \frac{1}{M_1 M_2} \sum_{i=1}^{M_1 M_2} \cos^{-1} \frac{\sum_{b=1}^{B} (x_{i,b} \cdot \hat{x}_{i,b})}{\sqrt{\sum_{b=1}^{B} x^2_{i,b}} \cdot \sqrt{\sum_{b=1}^{B} \hat{x}^2_{i,b}}}. \tag{36}$$

Here, $\hat{\boldsymbol{x}}_b$ and $\boldsymbol{x}_b$ represent the bth bands of the fused image and original image and M_1 and M_2 are the horizontal and vertical sizes of the image. $\sigma_{\hat{\boldsymbol{x}}_b \boldsymbol{x}_b}$ is the covariance between $\hat{\boldsymbol{x}}_b$ and $\boldsymbol{x}_b$, $m_{\hat{\boldsymbol{x}}_b}$ and $m_{\boldsymbol{x}_b}$ are their means, and $\sigma_{\hat{\boldsymbol{x}}_b}$ and $\sigma_{\boldsymbol{x}_b}$ are their standard deviations. The ideal values of the rmse, CC, UIQI, ERGAS, and SA are 0, 1, 1, 0, and 0, respectively.

The first series of experiments is performed on QuickBird images. The PAN and MS images were first resampled from 0.61 m and 2.44 m to 2.44 m and 9.76 m. Fig. 1(a) shows a resampled PAN image, and Fig. 1(b) shows the cubic interpolation version of resampled MS images (composition of bands 3, 2, and 1). The algorithms of Ehlers, PCA, GS, additive wavelet luminance proportional (AWLP) [17], and Li–Yang [35] and the proposed algorithm were implemented to make a comparative analysis. In order to effectively validate the advantages of the defined functions of the regularization parameters, the fusion model of (30) is also implemented. We call this method traditional parameter determination of a model-based method (TPDM). The termination threshold d in (23) was set to 10^{-7}, the parameter μ in (16) was set to 30, and $\lambda_{\mathrm{tradeoff}}$ was set to 60. The fusion results are shown in Fig. 1(c)–(h). Fig. 1(i) shows the original MS images. Apart from the fact that the TPDM result is blurred to some extent and the AWLP result appears darker, there is no great difference between the results from a visual inspection. We think that one reason for this may be that the images are 16 b. Table I shows the evaluation results for the *synthesis* property. The proposed algorithm produced better quantitative evaluation results than all other fusion methods in terms of all the five indices.

It should be noted that, although the evaluation results in bands 1 and 2 of the proposed method are a little poorer than those of TPDM, in terms of rmse, CC, and UIQI, it obtained much better results in band 4. In contrast, the results of TPDM in band 4 are very bad. Regarding the ERGAS and

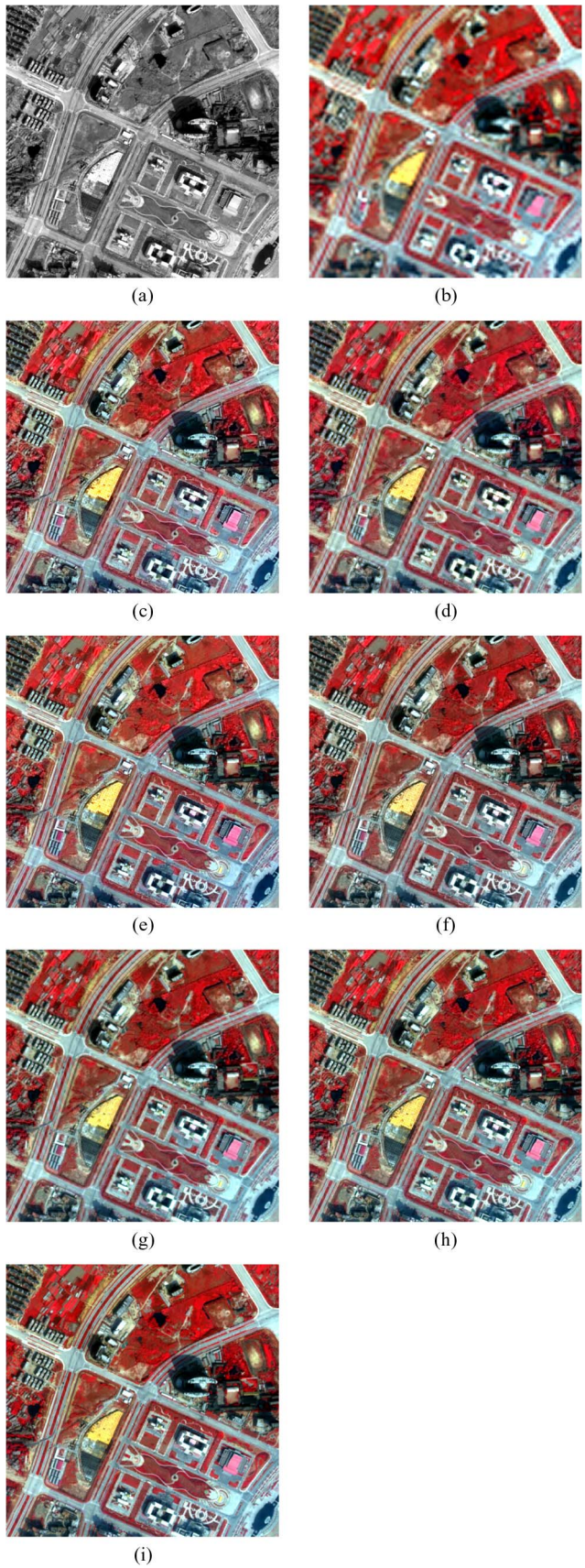

Fig. 1. Fusion results of the simulated QuickBird experiment (composed of near infrared, red, and green data bands). (a) Resampled PAN image. (b) Cubic interpolation of resampled MS image. (c) Ehlers fusion method. (d) AWLP fusion method. (e) GS fusion method. (f) Li–Yang fusion method. (g) TPDM fusion method. (h) Proposed fusion method. (i) Original MS image.

TABLE I
EVALUATION OF THE FUSION RESULTS IN THE SIMULATED QUICKBIRD EXPERIMENT (SYNTHESIS PROPERTY)

		Ehlers	AWLP	GS	Li-Yang	TPDM	Proposed
RMSE	B1	18.098	11.757	5.747	7.189	4.699	4.881
	B2	38.693	14.260	12.275	10.340	9.075	9.423
	B3	15.192	12.199	14.991	12.208	11.143	10.096
	B4	17.703	17.709	17.545	18.459	20.371	15.996
	Aver	22.422	13.981	12.640	12.049	11.322	10.099
CC	B1	0.922	0.884	0.951	0.961	0.968	0.964
	B2	0.942	0.956	0.961	0.972	0.977	0.975
	B3	0.955	0.971	0.959	0.977	0.976	0.980
	B4	0.969	0.963	0.963	0.969	0.962	0.972
	Aver	0.947	0.943	0.959	0.970	0.971	0.972
UIQI	B1	0.884	0.845	0.939	0.955	0.967	0.964
	B2	0.902	0.948	0.948	0.970	0.977	0.974
	B3	0.949	0.971	0.949	0.976	0.976	0.980
	B4	0.966	0.962	0.962	0.967	0.956	0.971
	Aver	0.925	0.931	0.950	0.967	0.969	0.972
ERGAS		1.244	0.801	0.767	0.727	0.718	0.612
SA		2.066	1.145	1.001	0.993	1.050	0.889

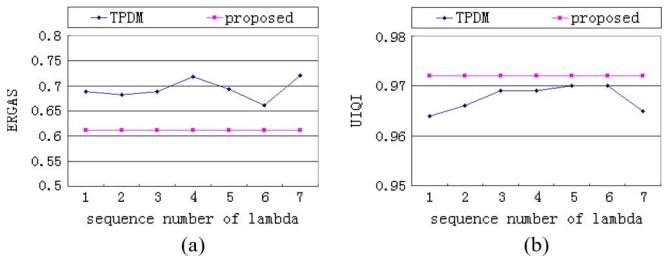

Fig. 2. Comparison of the proposed method with the TPDM method: (a) UIQI (band-averaged) values versus the regularization parameter and (b) ERGAS values versus the regularization parameter.

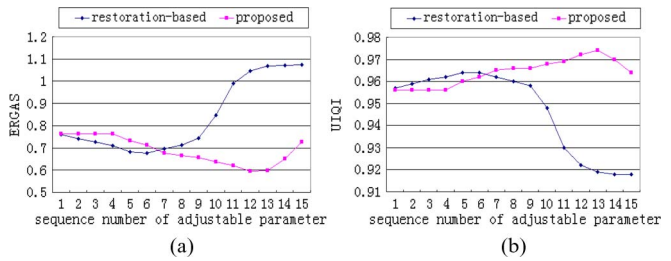

Fig. 3. Comparison of the restoration-based method with the proposed method. (a) UIQI values versus the adjustable parameter $\lambda_{\mathrm{tradeoff}}$. (b) ERGAS values versus the adjustable parameter $\lambda_{\mathrm{tradeoff}}$.

SA indices, the advantage of the proposed method is also very obvious. This validates that the proposed method has the performance to adaptively adjust the relative contributions in different bands, using the corresponding regularization parameters. A visualized comparison between these two methods in terms of the UIQI (band-averaged) and ERGAS indices is shown in Fig. 2. In the proposed method, $\lambda_{\mathrm{tradeoff}}$ is set to 60, and all other regularization parameters are determine adaptively. In the TPDM method, the parameter λ in (30) is respectively set to 0.0001, 0.0005, 0.001, 0.005, 0.01, 0.05, and 0.1.

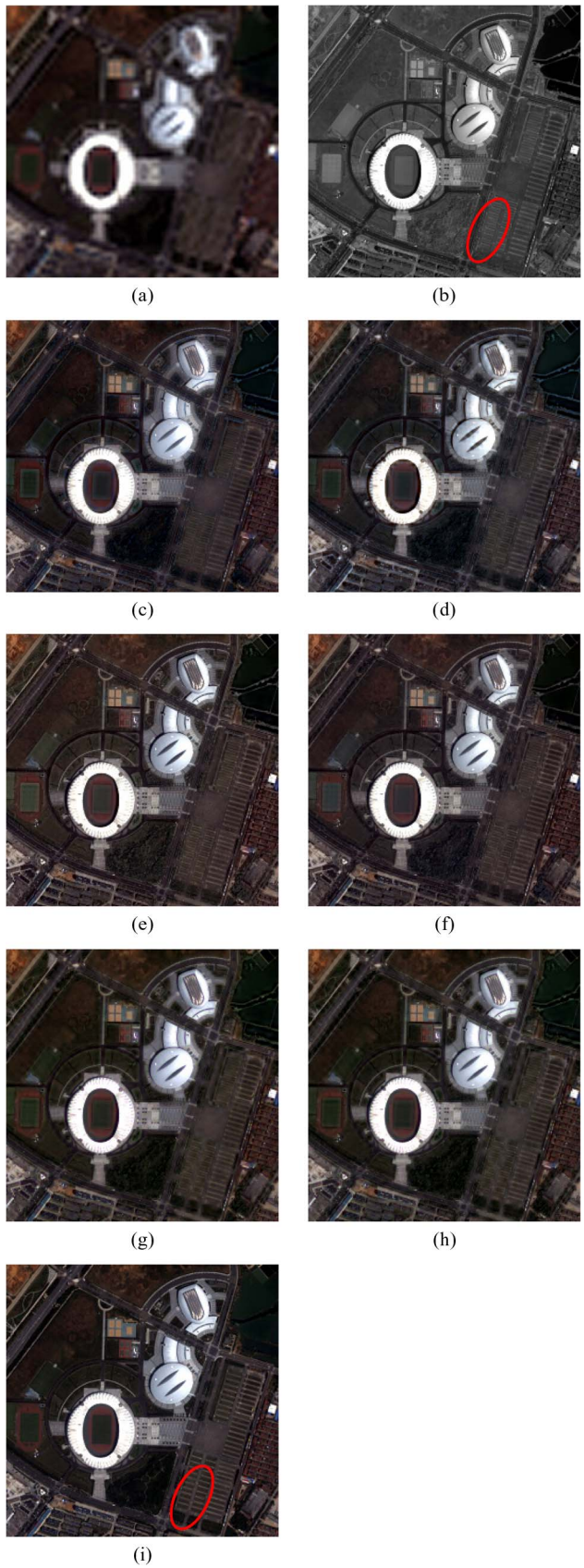

Fig. 4. Fusion results of the simulated IKONOS experiment (composed of near red, green and blue data bands). (a) Resampled PAN image. (b) Cubic interpolation of resampled MS image. (c) Ehlers fusion method. (d) AWLP fusion method. (e) GS fusion method. (f) Li–Yang fusion method. (g) TPDM fusion method. (h) Proposed method. (i) Original MS image.

TABLE II
EVALUATION OF THE FUSION RESULTS IN THE SIMULATED IKONOS EXPERIMENT (SYNTHESIS PROPERTY)

		Ehlers	AWLP	GS	Li-Yang	TPDM	Proposed
RMSE	B1	43.016	32.715	30.454	42.367	25.571	23.041
	B2	40.117	38.988	42.523	48.327	32.293	30.175
	B3	48.863	47.943	49.848	53.006	42.204	40.820
	B4	59.355	58.615	58.452	60.047	49.948	48.241
	Aver	47.838	44.565	45.319	50.937	37.504	35.569
CC	B1	0.968	0.965	0.968	0.971	0.978	0.981
	B2	0.978	0.976	0.974	0.980	0.984	0.986
	B3	0.974	0.970	0.971	0.977	0.979	0.979
	B4	0.953	0.947	0.947	0.960	0.962	0.964
	Aver	0.968	0.965	0.965	0.972	0.976	0.977
UIQI	B1	0.961	0.964	0.964	0.966	0.975	0.980
	B2	0.977	0.976	0.969	0.977	0.983	0.985
	B3	0.971	0.970	0.965	0.973	0.976	0.978
	B4	0.947	0.944	0.945	0.959	0.961	0.964
	Aver	0.964	0.963	0.961	0.969	0.974	0.977
ERGAS		2.089	1.953	1.989	2.215	1.657	1.580
SA		3.653	2.940	2.866	2.529	2.583	2.518

An additional experiment was implemented to compare the proposed method and the restoration-based method. In the experiment, the original MS image was first blurred by a 9×9 Gaussian kernel with a variance of 4 in order to the relieve the effects of aliasing [53] and then down sampled to obtain the degraded MS images. After that, the degraded versions were respectively fused using restoration-based and reconstruction-based methods. A series of values of the adjustable parameter $\lambda_{\text{tradeoff}}$, 0.001, 0.01, 0.05, 0.1, 0.5, 1, 5, 10, 20, 50, 100, 200, 500, 700, and 1000, is respectively tested in the experiment. The ERGAS and UIQI (band-averaged) evaluation values of the fused images against the adjustable parameter are respectively demonstrated in Fig. 3(a) and (b). Compared to the restoration-based method, the proposed method is able to obtain much better results and is less sensitive to the adjustable parameter. The main reason is that the restoration-based method transfers errors of interpolation into the fusion process. The proposed method, however, avoids this error accumulation.

The simulated experimental results of the IKONOS images are shown in Fig. 4, and Table II shows the quantitative indices of the different fusion methods. In terms of the rmse, ERGAS, and SA indices, the evaluation results of all the fusion methods are much poorer than those in the QuickBird experiments. The main reason for this is that the PAN image that was used lost some detailed information which appears in the original MS images. Please see the labeled regions in Fig. 4(b) and (i). Relatively, the proposed method outperforms the other fusion methods in terms of all the indices.

B. Experiments on Real Images

In this section, the proposed method was tested on real observed images. Fig. 5(a) and (b) shows the original PAN image and the interpolated version of MS QuickBird images.

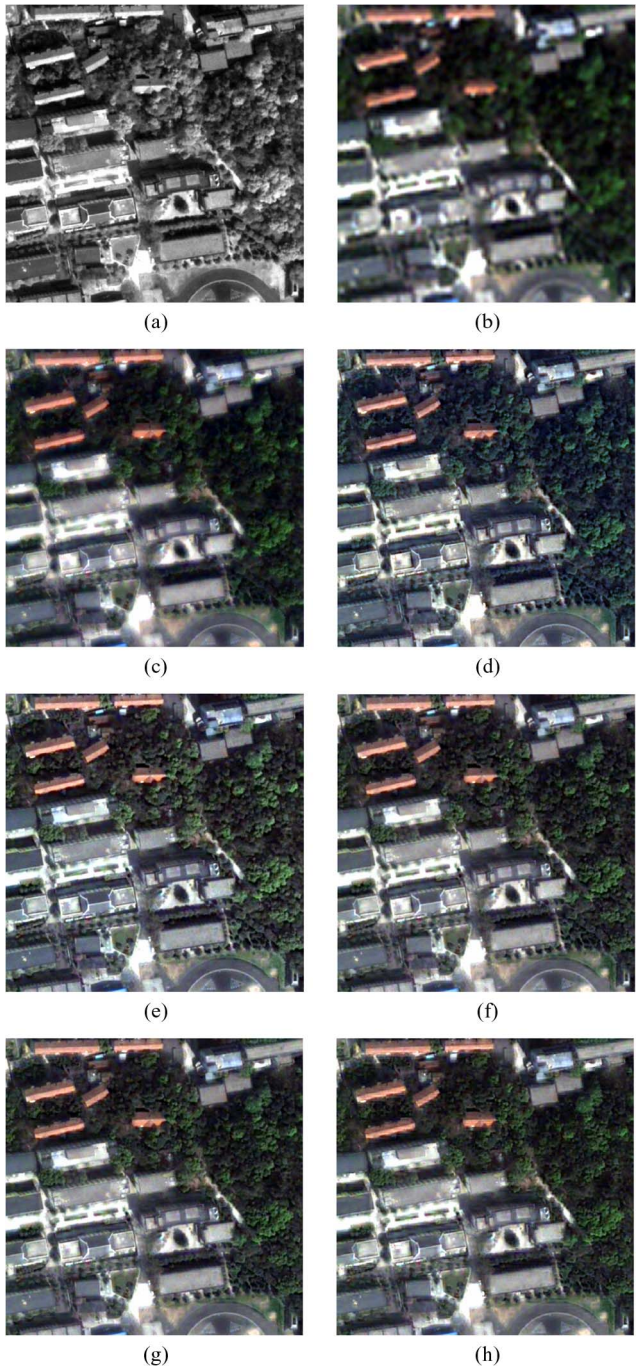

Fig. 5. Fusion results of the real QuickBird experiment (composed of near red, green and blue data bands). (a) PAN image. (b) Cubic interpolation of MS image. (c) Ehlers fusion method. (d) AWLP fusion method. (e) GS fusion method. (f) TPDM fusion method. (g) Proposed method with $\lambda_{\text{tradeoff}} = 2$. (h) Proposed method with $\lambda_{\text{tradeoff}} = 10$.

Since the Li–Yang method desires additional HR MS images to construct a dictionary [35], it is unable to be implemented in the real experiments. The fused results of the Ehlers, AWLP, GS, and TPDM methods are respectively shown in Fig. 5(c)–(f), and Fig. 5(g) and (h) shows the results of the proposed method, with $\lambda_{\text{tradeoff}} = 2$ and $\lambda_{\text{tradeoff}} = 10$, respectively. Here, the Huber parameter μ is set to 1. By visual comparison, the Ehlers method shows better performance of spectral fidelity

TABLE III
EVALUATION RESULTS OF THE REAL QUICKBIRD EXPERIMENT (CONSISTENCY PROPERTY)

		Ehlers	AWLP	GS	TPDM	Proposed $\lambda_{\text{tradeoff}}$=2	Proposed $\lambda_{\text{tradeoff}}$=10
RMSE	B1	8.008	7.894	8.239	6.321	4.601	2.157
	B2	10.103	10.592	18.168	12.842	10.561	4.995
	B3	15.435	6.840	18.741	12.800	10.524	4.983
	B4	22.479	8.527	22.688	23.487	21.203	10.159
	Aver	14.006	8.464	16.959	13.863	11.722	5.574
CC	B1	0.982	0.956	0.940	0.970	0.983	0.996
	B2	0.986	0.981	0.931	0.971	0.980	0.995
	B3	0.989	0.993	0.935	0.974	0.982	0.996
	B4	0.991	0.994	0.956	0.955	0.963	0.991
	Aver	0.987	0.981	0.941	0.967	0.977	0.995
UIQI	B1	0.979	0.951	0.934	0.968	0.982	0.996
	B2	0.986	0.979	0.926	0.969	0.979	0.995
	B3	0.987	0.992	0.930	0.972	0.981	0.996
	B4	0.988	0.994	0.955	0.954	0.962	0.991
	Aver	0.985	0.979	0.937	0.966	0.976	0.994
ERGAS		1.398	0.748	1.616	1.354	1.170	0.558
SA		2.227	0.242	0.878	0.873	0.839	0.408

(a) (b) (c) (d)

Fig. 6. Sensitivity analysis of the Huber parameter μ. (a) $\lambda_{\text{tradeoff}} = 2$ and $\mu = 100$. (b) $\lambda_{\text{tradeoff}} = 2$ and $\mu = 1$. (c) $\lambda_{\text{tradeoff}} = 10$ and $\mu = 100$. (d) $\lambda_{\text{tradeoff}} = 10$ and $\mu = 1$.

than other existed methods, but the image is oversmoothed. The visual equality of the AWLP image is not satisfactory because of the color distortion, which is obvious on vegetation regions. It is interesting that the AWLP method obtains good evaluation values from Table III. In particular, the SA is very small. Therefore, quantitative evaluation does not completely agree with visual judgment for the AWLP method here. However, the proposed method is competitive in terms of both visual and quantitative evaluations. Moreover, the adjustable function of $\lambda_{\text{tradeoff}}$ is effectively embodied. When it is set a smaller value $(\lambda_{\text{tradeoff}} = 2)$, the fused image is clearer with weaker spectral fidelity, and when it is set a larger value $(\lambda_{\text{tradeoff}} = 10)$, the result has better spectral consistency but lower image definition.

The function of the edge-preserving Huber–Markov prior model (12) was tested, and the sensitivity analysis of the parameter μ is shown in Fig. 6. When $\lambda_{\text{tradeoff}}$ is relatively small, the spatial structures desired by the MS images can be sufficiently extracted from the PAN image; therefore, the fusion result is not sensitive to the Huber parameter μ. Oppositely, if the spectral maintenance is strictly demanded in the fusion process, $\lambda_{\text{tradeoff}}$ should be set to a larger value. Similar to the Gauss–Markov and Laplacian models, the Huber model also leads to smoothed results when μ is large in this case. However,

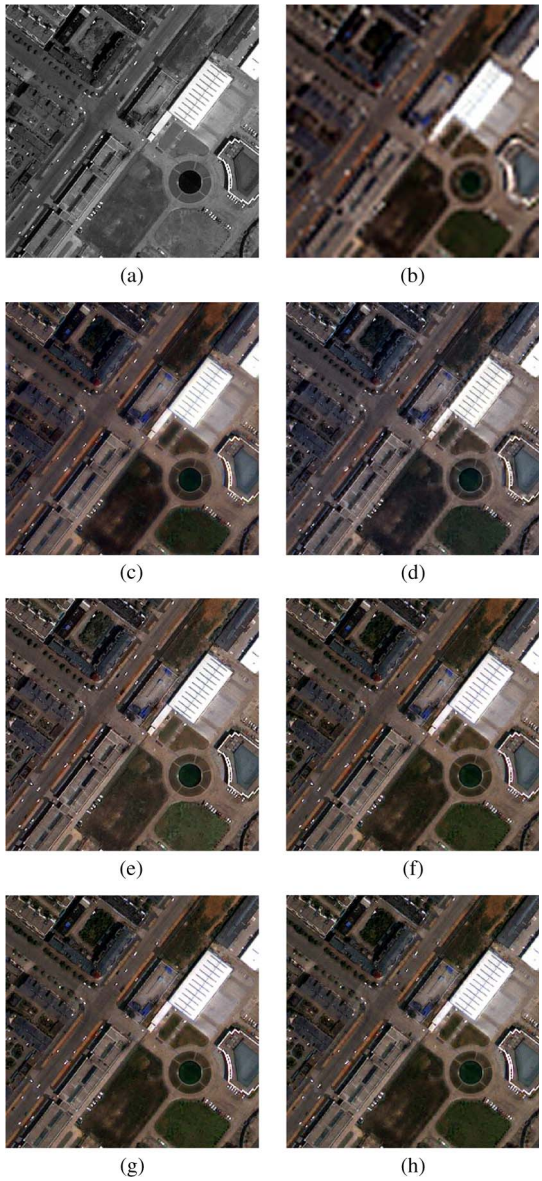

(a) (b) (c) (d) (e) (f) (g) (h)

Fig. 7. Fusion results of the real IKONOS experiment (composed of near red, green and blue data bands). (a) PAN image. (b) Cubic interpolation of MS image. (c) Ehlers fusion method. (d) AWLP fusion method. (e) GS fusion method. (f) TPDM fusion method. (g) Proposed method with $\lambda_{\text{tradeoff}} = 2$. (h) Proposed method with $\lambda_{\text{tradeoff}} = 10$.

the smooth problem can be well solved by adjusting μ to a small value. This is an important advantage of the Huber–Markov model compared to the Gauss–Markov and Laplacian models.

In the last series of experiments, the fusion methods were applied to real IKONOS images. The MS image [see Fig. 7(b)] was fused with the corresponding PAN image [see Fig. 7(a)] using the aforementioned methods. The fused results are respectively shown in Fig. 7(c)–(h). Again, the fused image of the Ehlers method is oversmoothed, and the AWLP method leads to color distortion from visual judgments. Quantitative evaluation in Table IV shows that the AWLP method never produces good values as in the QuickBird experiments. The model-based TPDM method outperforms all other existed methods but is inferior compared to the proposed method. Fig. 8 shows the horizontal profiles of digital values on several degraded versions of images in Fig. 7. It is seen that the Ehlers method

TABLE IV
EVALUATION RESULTS OF THE REAL IKONOS EXPERIMENT (CONSISTENCY PROPERTY)

		Ehlers	AWLP	GS	TPDM	Proposed $\lambda_{\text{tradeoff}}=2$	Proposed $\lambda_{\text{tradeoff}}=10$
RMSE	B1	51.458	24.945	24.446	9.960	7.500	3.311
	B2	24.347	39.155	37.787	20.190	17.169	7.749
	B3	38.637	46.034	42.045	17.509	14.552	6.530
	B4	25.162	47.014	42.915	24.403	21.355	9.696
	Aver	34.901	39.287	36.798	18.016	15.144	6.822
CC	B1	0.984	0.965	0.977	0.995	0.997	1.000
	B2	0.989	0.965	0.979	0.992	0.995	0.999
	B3	0.991	0.957	0.976	0.995	0.997	0.999
	B4	0.986	0.940	0.950	0.984	0.988	0.998
	Aver	0.987	0.957	0.971	0.992	0.994	0.999
UIQI	B1	0.979	0.965	0.934	0.968	0.997	0.996
	B2	0.986	0.965	0.926	0.969	0.993	0.995
	B3	0.987	0.956	0.930	0.972	0.996	0.995
	B4	0.988	0.939	0.955	0.954	0.988	0.990
	Aver	0.985	0.956	0.937	0.966	0.993	0.994
ERGAS		1.587	1.667	1.552	0.763	0.647	0.292
SA		2.923	1.563	1.603	0.331	0.317	0.149

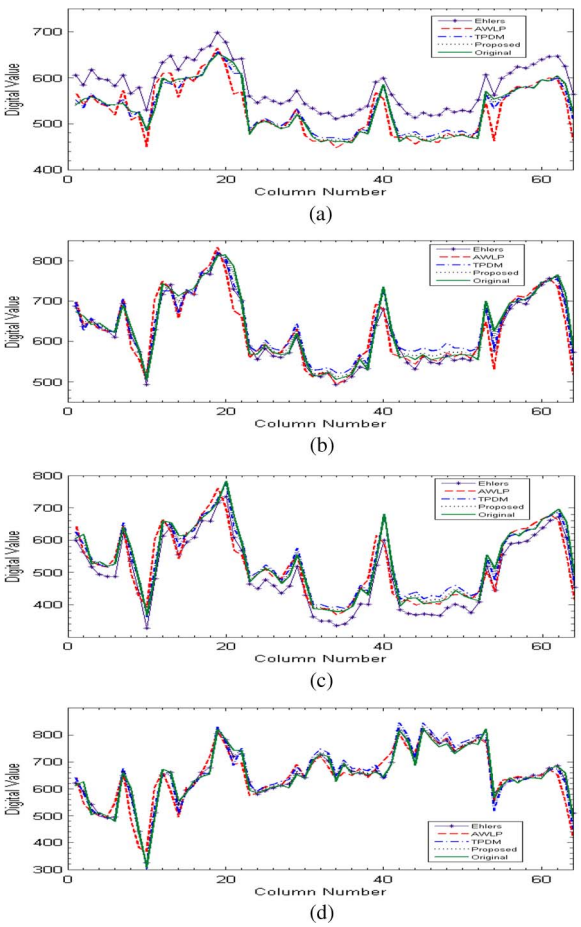

Fig. 8. Horizontal profiles of digital values of the 45th line on the degraded versions of Ehlers, AWLP, TPDM, and proposed results and original MS images in Fig. 7(a)–(d): Bands 1, 2, 3, and 4.

has good performance to retain the curve shape but has great absolute errors. This is the reason why it produces high CC values but bad SA values. The curves of the proposed method are the most proximal to those of the original MS images.

VII. CONCLUSION

This paper presents an adjustable model-based method for the MS-PAN image fusion problem. The proposed method has been tested using QuickBird and IKONOS images. The fused images were evaluated using the quality indices of mean square error, CC, UIQI, ERGAS, and SA, in terms of both synthesis property and consistency property. Evaluation results confirmed that the proposed method outperforms the fusion methods of Ehlers, AWLP, GS, Li–Yang, and TPDM. Nevertheless, further work can potentially expand the method to incorporate a fast optimization algorithm and use tensor representation [54] to improve the matrix-based fusion model.

REFERENCES

[1] C. P. Ruiz and F. J. A. Lopez, "Restoring SPOT images using PSF-derived deconvolution filters," *Int. J. Remote Sens.*, vol. 23, no. 12, pp. 2379–2391, Jun. 2002.
[2] B. J. Kang and K. R. Park, "Real-time image restoration for iris recognition systems," *IEEE Trans. Syst., Man, Cybern. B, Cybern.*, vol. 37, no. 6, pp. 1555–1566, Dec. 2007.
[3] K. Panetta, S. Agaian, Y. Zhou, and E. J. Wharton, "Parameterized logarithmic framework for image enhancement," *IEEE Trans. Syst., Man, Cybern. B, Cybern.*, vol. 41, no. 2, pp. 460–473, Apr. 2010.
[4] H. Shen, L. Zhang, B. Huang, and P. Li, "A MAP approach for joint motion estimation, segmentation, super resolution," *IEEE Trans. Image Process.*, vol. 16, no. 2, pp. 479–490, Feb. 2007.
[5] M. K. Ng, H. Shen, S. Chaudhuri, and A. C. Yau, "Zoom-based super-resolution reconstruction approach using prior total variation," *Opt. Eng.*, vol. 46, no. 12, p. 127 003, Dec. 2007.
[6] M. V. Joshi, S. Chaudhuri, and R. Panuganti, "A learning-based method for image super-resolution from zoomed observations," *IEEE Trans. Syst., Man, Cybern. B, Cybern.*, vol. 35, no. 3, pp. 527–537, Jun. 2005.
[7] C. Pohl and J. L. van Genderen, "Multisensor image fusion remote sensing: Concepts, methods and applications," *Int. J. Remote Sens.*, vol. 19, no. 5, pp. 823–854, Mar. 1998.
[8] P. S. Chavez, Jr., S. C. Sides, and J. A. Anderson, "Comparison of three different methods to merge multiresolution and multispectral data. Landsat TM and SPOT panchromatic," *Photogram. Eng. Remote Sens.*, vol. 57, no. 3, pp. 295–303, Mar. 1991.
[9] V. K. Shettigara, "A generalized component substitution technique for spatial enhancement of multispectral images using a higher resolution data set," *Photogram. Eng. Remote Sens.*, vol. 58, no. 5, pp. 561–567, 1992.
[10] X. Li, Y. Pang, and Y. Yuan, "L1-norm-based 2D PCA," *IEEE Trans. Syst., Man, Cybern. B, Cybern.*, vol. 40, no. 4, pp. 1170–1175, Aug. 2010.
[11] Y. Pang, D. Tao, Y. Yuan, and X. Li, "Binary two-dimensional PCA," *IEEE Trans. Syst., Man, Cybern. B, Cybern.*, vol. 38, no. 4, pp. 1176–1180, Aug. 2008.
[12] M. Gonzalez-Audicana, X. Otazu, O. Fors, and J. Alvarez-Mozos, "A low computational-cost method to fuse IKONOS images using the spectral response function of its sensors," *IEEE Trans. Geosci. Remote Sens.*, vol. 44, no. 6, pp. 1683–1691, Jun. 2006.
[13] Y. Zhang, "A new automatic approach for effectively fusing Landsat 7 as well as IKONOS images," in *Proc. IGARSS*, Toronto, ON, Canada, 2002, pp. 2429–2431.
[14] C. A. Laben and B. V. Brower, "Process for enhancing the spatial resolution of multispectral imagery using pan-sharpening," U.S. Patent 6 011 875, Jan. 4, 2000.
[15] B. Aiazzi, L. Alparone, S. Baronti, A. Garzelli, and M. Selva, "MTF-tailored multiscale fusion of high-resolution MS and pan imagery," *Photogramm. Eng. Remote Sens.*, vol. 72, no. 5, pp. 591–596, May 2006.
[16] B. Aiazzi, L. Alparone, S. Baronti, and A. Garzelli, "Context-driven fusion of high spatial and spectral resolution images based on oversampled multiresolution analysis," *IEEE Trans. Geosci. Remote Sens.*, vol. 40, no. 10, pp. 2300–2312, Oct. 2002.

[17] X. Otazu, M. Gonzalez-Audicana, O. Fors, and J. Nunez, "Introduction of sensor spectral response into image fusion methods. Application to wavelet-based methods," *IEEE Trans. Geoscience and Remote Sensing*, vol. 43, no. 10, pp. 2376–2385, Oct. 2005.
[18] M. Choi, R. Y. Kim, M. R. Nam, and H. O. Kim, "Fusion of multispectral and panchromatic satellite images using the curvelet transform," *IEEE Geosci. Remote Sens. Lett.*, vol. 2, no. 2, pp. 136–140, Apr. 2005.
[19] H. Song, S. Yu, L. Song, and X. Yang, "Fusion of multispectral and panchromatic satellite images based on contourlet transform and local average gradient," *Opt. Eng.*, vol. 46, p. 020502, Feb. 2007.
[20] C. Thomas, T. Ranchin, L. Wald, and J. Chanussot, "Synthesis of multispectral images to high spatial resolution: A critical review of fusion methods based on remote sensing physics," *IEEE Trans. Geosci. Remote Sens.*, vol. 46, no. 5, pp. 1301–1312, May 2008.
[21] U. Pradhan and D. W. Holcomb, "Optimizing the high-pass filter addition technique for image fusion," *Photogramm. Eng. Remote Sens.*, vol. 74, no. 9, pp. 1107–1118, Sep. 2008.
[22] J. G. Liu, "Smoothing filter-based intensity modulation: A spectral preserve image fusion technique for improving spatial details," *Int. J. Remote Sens.*, vol. 21, no. 18, pp. 3461–3472, Dec. 2000.
[23] M. Ehlers, "Spectral characteristics preserving image fusion based on Fourier domain filtering," in *Proc. SPIE-Remote Sens. Environ. Monit., GIS Appl., Geol. IV*, Maspalomas, Gran Canaria, Spain, 2004.
[24] H. Gross and J. Schott, "Application of spectral mixture analysis and image fusion techniques for image sharpening," *Remote Sens. Environ.*, vol. 63, no. 2, pp. 85–94, Feb. 1998.
[25] M. T. Eismann and R. C. Hardie, "Application of the stochastic mixing model to hyperspectral resolution enhancement," *IEEE Trans. Geosci. Remote Sens.*, vol. 42, no. 9, pp. 1924–1933, Sep. 2004.
[26] S. C. Park, M. K. Park, and M. G. Kang, "Super-resolution image reconstruction: A technical overview," *IEEE Signal Process. Mag.*, vol. 20, no. 3, pp. 21–36, May 2003.
[27] M. L. S. Aguena and N. Mascarenhas, "Multispectral image data fusion using projections onto convex sets techniques," in *Proc. XV Braz. Symp. Comput. Graph. Image Process.*, 2002, pp. 76–82.
[28] R. C. Hardie, M. T. Eismann, and G. L. Wilson, "MAP estimation for hyperspectral image resolution enhancement using an auxiliary sensor," *IEEE Trans. Image Process.*, vol. 13, no. 9, pp. 1174–1184, Sep. 2004.
[29] Y. Zhang, S. De Backer, and P. Scheunders, "Noise-resistant wavelet-based Bayesian fusion of multispectral and hyperspectral images," *IEEE Trans. Geosci. Remote Sens.*, vol. 47, no. 11, pp. 3834–3843, Nov. 2009.
[30] R. Molina, M. Vega, J. Mateos, and A. K. Katsaggelos, "Variational posterior distribution approximation Bayesian super resolution reconstruction of multispectral images," *Appl. Comput. Harmon. Anal., special issue on "Mathematical Imaging," Part II*, vol. 24, no. 2, pp. 251–267, Mar. 2008.
[31] M. V. Joshi, L. Bruzzone, and S. Chaudhuri, "A model-based approach to multiresolution fusion remotely sensed images," *IEEE Trans. Geosci. Remote Sens.*, vol. 44, no. 9, pp. 2549–2562, Sep. 2006.
[32] L. Joshi and A. Jalobeanu, "MAP estimation for multiresolution fusion remotely sensed images using an IGMRF prior mode," *IEEE Trans. Geosci. Remote Sens.*, vol. 48, no. 3, pp. 1245–1255, Mar. 2010.
[33] Z. Li and H. Leung, "Fusion of multispectral and panchromatic images using a restoration-based method," *IEEE Trans. Geosci. Remote Sens.*, vol. 47, no. 5, pp. 1482–1491, May 2009.
[34] H. Aans, J. R. Sveinsson, A. A. Nielsen, T. Bovith, and J. A. Benediktsson, "Model-based satellite image fusion," *IEEE Trans. Geosci. Remote Sens.*, vol. 46, no. 5, pp. 1336–1346, May 2008.
[35] S. Li and B. Yang, "A new pan-sharpening method using a compressed sensing technique," *IEEE Trans. Geosci. Remote Sens.*, vol. 49, no. 2, pp. 738–746, Feb. 2011.
[36] G. A. Boggione, E. G. Pires, P. A. Santos, and L. M. G. Fonseca, "Simulation of a panchromatic band by spectral combination of multispectral ETM+ bands," in *Proc. ISRSE*, Honolulu, HI, 2003.
[37] M. Vega, J. Mateos, R. Molina, and A. K. Katsaggelos, "Super-resolution of multispectral images," *Comput. J.*, vol. 52, no. 1, pp. 153–167, Jan. 2009.
[38] M. K. Ng, W. C. Kwan, and R. H. Chan, "A fast algorithm for high-resolution color image reconstruction with multisensors," in *Proc. Numer. Anal. Appl.*, vol. 1988, *Lecture Notes Computer Science*, pp. 615–627.
[39] S. Farsiu, M. Elad, and P. Milanfar, "Multiframe demosaicing and super-resolution of color images," *IEEE Trans. Image Process.*, vol. 15, no. 1, pp. 141–159, Jan. 2006.
[40] M. K. Ng, H. Shen, L. Zhang, and E. Lam, "A total variation based super-resolution reconstruction algorithm for digital video," *EURASIP J. Adv. Signal Process.*, vol. 2007, p. 74 585, 2007.
[41] R. R. Schultz and R. L. Stevenson, "Extraction of high-resolution frames from video sequences," *IEEE Trans. Image Process.*, vol. 5, no. 6, pp. 996–1011, June 1996.
[42] D. Jing and C. Zhijun, "Study on adjustable image fusion method for remote sensing," *Acta Opt. Sin.*, vol. 5, pp. 25 593–25 597, May 2005.
[43] T. M. Tu, Y. C. Lee, C. P. Chang, and P. S. Huang, "Adjustable intensity-hue-saturation and Brovey transform fusion technique for IKONOS/QuickBird imagery," *Opt. Eng.*, vol. 44, p. 116 201, Nov 2005.
[44] N. Nguyen, P. Milanfar, and G. Golub, "Efficient generalized cross-validation with applications to parametric image restoration and resolution enhancement," *IEEE Trans. Image Process.*, vol. 10, no. 9, pp. 1299–1308, Sep. 2001.
[45] N. K. Bose, S. Lertrattanapanich, and J. Koo, "Advances superresolution using L-curve," in *Proc. IEEE Int. Symp. Circuits Syst.*, 2001, pp. 433–436.
[46] D. Krawczyk-StańDo and M. Rudnicki, "Regularization parameter selection discrete ill-posed problems—The use of the U-curve," *Int. J. Appl. Math. Comput. Sci.*, vol. 17, no. 2, pp. 157–164, Jun. 2007.
[47] Q. Yuan, L. Zhang, H. Shen, and P. Li, "Adaptive multiple-frame image super-resolution based on U-curve," *IEEE Trans. Image Process.*, vol. 19, no. 12, pp. 3157–3170, Dec. 2010.
[48] M. G. Kang and A. K. Katsaggelos, "General choice of the regularization functional regularized image restoration," *IEEE Trans. Image Process.*, vol. 4, no. 5, pp. 594–602, May 1995.
[49] E. S. Lee and M. G. Kang, "Regularized adaptive high-resolution image reconstruction considering inaccurate subpixel registration," *IEEE Trans. Image Process.*, vol. 12, no. 7, pp. 826–837, July 2003.
[50] H. Hu and L. P. Kondi, "An image super-resolution algorithm for different error levels per frame," *IEEE Trans. Image Process.*, vol. 15, no. 3, pp. 592–603, Mar. 2006.
[51] T. Ranchin, B. Aiazzi, L. Alparone, S. Baronti, and L. Wald, "Image fusion-The ARSIS concept and some successful implementation schemes," *ISPRS J. Photogramm. Remote Sens.*, vol. 58, no. 1/2, pp. 4–18, Jun. 2003.
[52] Z. J. Wang, D. Ziou, C. Armenakis, D. Li, and Q. Q. Li, "A comparative analysis of image fusion methods," *IEEE Trans. Geosci. Remote Sens.*, vol. 43, no. 6, pp. 1391–1402, Jun. 2005.
[53] H. S. Stone, M. T. Orchard, E.-C. Chang, and S. A. Martucci, "A fast direct Fourier-based algorithm for subpixel registration of images," *IEEE Trans. Geosci. Remote Sens.*, vol. 39, no. 10, pp. 2235–2243, Oct. 2001.
[54] X. Li, S. Lin, S. Yan, and D. Xu, "Discriminant locally linear embedding with high-order tensor data," *IEEE Trans. Syst., Man, Cybern. B, Cybern.*, vol. 38, no. 2, pp. 342–352, Apr. 2008.

Liangpei Zhang (M'06–SM'08) received the B.S. degree in physics from Hunan Normal University, Changsha, China, in 1982, the M.S. degree in optics from the Xi'an Institute of Optics and Precision Mechanics, Chinese Academy of Sciences, Xi'an, China, in 1988, and the Ph.D. degree in photogrammetry and remote sensing from Wuhan University, Wuhan, China, in 1998.

He is currently the Head of the Remote Sensing Division, State Key Laboratory of Information Engineering in Surveying, Mapping, and Remote Sensing, Wuhan University. He is also a "Chang-Jiang Scholar" Chair Professor appointed by the Ministry of Education of China. He is currently a Principal Scientist for the China State Key Basic Research Project (2011–2016) appointed by the Ministry of National Science and Technology of China to lead the remote sensing program in China. He has more than 240 research papers. He is the holder of five patents. His research interests include hyperspectral remote sensing, high-resolution remote sensing, image processing, and artificial intelligence.

Dr. Zhang is a fellow of the IEE (the institution of electrical engineers), Executive Member (Board of Governor) of the China National Committee of International Geosphere—Biosphere Programme, Executive Member of the China Society of Image and Graphics, etc. He regularly serves as a Cochair of the series SPIE (the international society for optics and photonics) Conferences on Multispectral Image Processing and Pattern Recognition, Conference on Asia Remote Sensing, and many other conferences. He edits several conference proceedings, issues, and geoinformatics symposiums. He also serves as an Associate Editor of the *International Journal of Ambient Computing and Intelligence, International Journal of Image and Graphics, International Journal of Digital Multimedia Broadcasting, Journal of Geo-spatial Information Science, and Journal of Remote Sensing*.

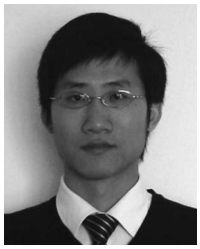

Huanfeng Shen (M'10) received the B.S. degree in engineering of surveying and mapping and the Ph.D. degree in photogrammetry and remote sensing from Wuhan University, Wuhan, China, in 2002 and 2007, respectively.

He served as a Research Assistant at the Department of Mathematics, Hong Kong Baptist University, Kowloon, Hong Kong, from 2006 to 2007. He is currently a Professor at the School of Resource and Environmental Science, Wuhan University. His research interests include image processing and fusion, remote sensing application, and global change. He has published more than 60 research papers. He has been supported by several talent programs, such as the New Century Excellent Talents by the Ministry of Education of China (2011), Hubei Science Fund for Distinguished Young Scholars (2011), etc.

Wei Gong received the B.S. degree in photonics engineering from the Huazhong University of Science and Technology (HUST), Wuhan, China, in 1993, the M.S. degree in electronics from the Chinese Academic of Sciences, Lanzhou, China, in 1996, and the Ph.D. degree in physical electronics from HUST, in 1999.

He served as an Assistant Professor in Hampton University, Hampton, Virginia, United States from 2002 to 2004. He is currently a Professor with the State Key Laboratory of Information Engineering in Surveying, Mapping, and Remote Sensing, Wuhan University, Wuhan. He is mainly engaged in teaching and research of new laser, optical technology, and its remote sensing applications and has made certain achievement in atmospheric lidar and optical remote sensing. Since 2005, he has presided over quiet a few projects, which amounted to 20 million national research funding. In the recent five years, he had more than 60 scientific papers accepted and published, 13 patents opened and authorized, and two books copublished. In view of the aforementioned achievement, he was selected as one of the "New Century Excellent Talents" in 2007, "Luojia Scholars," and "Chutian Scholars" in 2010.

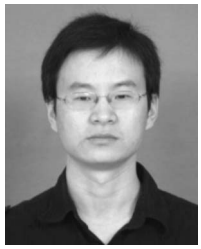

Hongyan Zhang received the B.S. degree in geographic information system and the Ph.D. degree in photogrammetry and remote sensing from Wuhan University, Wuhan, China, in 2005 and 2010, respectively.

Since 2010, he has been an Assistant Professor with the State Key Laboratory of Information Engineering in Surveying, Mapping, and Remote Sensing, Wuhan University. His current research interests focus on image reconstruction and remote sensing image processing.